Applied Catalysis B: Environmental 338 (2023) 123068

Contents lists available at ScienceDirect

Applied Catalysis B: Environmental

journal homepage: www.elsevier.com/locate/apcatb

Selective two-electron electrocatalytic conversion of 5-Hydroxymethylfurfural boosting hydrogen production under neutral condition over Co$(OH)_2$-CeO_2 catalyst

Yanan Xie, Lingzhi Sun, Xun Pan, Zhaoyu Zhou, Guohua Zhao *

Key Laboratory of Spine and Spinal Cord Injury Repair and Regeneration, Ministry of Education, Tongji Hospital, School of Chemical Science and Engineering, Tongji University, Shanghai 200092, China

ARTICLE INFO

Keywords:
Selective electrocatalysis
Hydrogen production
Value-added chemicals
In situ Raman spectroscopy

ABSTRACT

The coupling of electrocatalytic oxidation of biomass derivatives with hydrogen evolution reaction (HER) is a promising strategy to promote hydrogen production, but it is extremely challenging to control the mild electrocatalytic conversion of biomass to high value-added chemicals simultaneously. A Co$(OH)_2$-CeO_2 self-supported catalyst is constructed and used as anode for selective electrocatalytic conversion of biomass derivative 5-hydroxymethylfurfural (HMF) coupled with HER in two-chamber electrolysis system. The adjusting of pH and potential regulates the oxidation ability of hydroxyl and aldehyde groups, achieving selective two-electron electrocatalytic conversion of HMF to 2-furancarboxylic acid (HMFCA) with a selectivity of 89.4%. In situ Raman spectroscopy reveals that the evolution of Co multivalent active species at different electrolysis conditions is key to the selective oxidation of HMF. In addition, the hydrogen production coupled with selective electrocatalytic conversion of HMF is 4.1 times that of the water splitting system, revealing its potential in developing clean energy.

1. Introduction

The increasingly serious over-exploitation and use of fossil fuels, the ensuing energy crisis and environmental pollution have become urgent problems to be solved. Finding clean and sustainable new energy sources has become a research hotspot. It is a potential energy strategy to use wind energy, solar energy and tidal energy to generate electricity for hydrogen production [1]. However, due to the high energy consumption caused by the high overpotential of anodic water oxidation and the possible generation of destructive reactive oxygen species, as well as the risk of hydrogen/oxygen mixed explosion, the commercialization of electrolytic hydrogen production is hindered [2,3]. Therefore, it is necessary to find an efficient and safe new hydrogen production system to achieve large-scale hydrogen production. Biomass and its derivatives are the only renewable resources that can meet the huge demand for chemicals on the earth, and the oxidation potential of smallest molecule derivatives is lower than 1.0 V. Therefore, the use of thermodynamically more favorable oxidation reaction of biomass derivative instead of water oxidation coupling hydrogen production can effectively reduce the hydrogen production overpotential [4–6].

5-Hydroxymethylfurfural (HMF) is an important biological platform molecule obtained by dehydration of C6 compounds such as fructose [7,8]. HMF contains two different reactive functional groups, aldehyde (-CHO) and hydroxyl (-COH), which can be oxidized to a variety of high value-added derivatives, such as 2,5-diformylfuran (DFF), 5-hydroxymethyl-2-furancarboxylic acid (HMFCA), 5-formyl-2-furancarboxylic acid (FFCA) and 2,5-furandicarboxylic acid (FDCA) [9–11]. To date, Ni-based electrocatalysts have been widely used in the study of electrocatalytic conversion of HMF to FDCA, achieving a Faraday efficiency of nearly 100% for FDCA on materials such as Ni_3S_2, Ni_2P and CoFe@NiFe-LDH [12–15]. However, the relatively strong oxidation ability of Ni species makes it easy for functional groups such as -CHO and -OH to be further oxidized. The mild oxidation of HMF is extremely challenging, and the two-electron oxidation to HMFCA or DFF is less studied. Reactions corresponding to the conversion of HMF into HMFCA and DFF are shown in reaction 1–2. In addition to the intrinsic performance of the electrocatalyst, the reaction rate of the electrochemical reaction, the selectivity and yield of the product can be adjusted by the nature of the electrolyte. Previously, electrocatalytic conversion of HMF was mostly carried out in a strong alkaline solution, which was

* Corresponding author.
E-mail address: g.zhao@tongji.edu.cn (G. Zhao).

https://doi.org/10.1016/j.apcatb.2023.123068
Received 28 February 2023; Received in revised form 30 June 2023; Accepted 2 July 2023
Available online 3 July 2023

conducive to the formation of high-valent active metal species. This requires more sophisticated process equipment and more cost input in the industrial production process. The related research under neutral condition has more practical research significance, but the difficulty in generating reactive active species under neutral conditions limits the activity of electrocatalytic conversion [16,17]. Based on this, the development of a mild and efficient method for selective electrocatalytic conversion of HMF under neutral conditions is of great significance for promoting industrial application.

HMF into HMFCA and H_2:

$$HMF + H_2O \rightarrow HMFCA + H_2 \quad (1)$$

HMF into DFF and H_2:

$$HMF + H_2O \rightarrow DFF + H_2 \quad (2)$$

Co-based electrocatalysts have been studied in the oxidation of glycerol, ethanol and methanol because of their mild redox chemical ability, high electrocatalytic performance, good stability and large cost advantages [18–21]. In our previous work of selective electrocatalytic conversion of HMF, it was also shown that the Co^{3+} species effectively reduced the initial potential of HMF oxidation, but the low conductivity of Co-based catalysts limits their catalytic activity [15,22]. Some studies have reported that the performance of binary or ternary metal oxides is usually better than that of single oxides, and the construction of heterostructures with synergistic effects containing different functional species is considered to be a common way to improve performance [23–25]. Cerium oxide (CeO_2) is an important rare earth metal oxide. Due to its unique properties, it has been widely used as an accelerator to improve the catalytic performance of electrocatalysts. Heterostructures based on CeO_2 (e.g., $Ni(OH)_2$-CeO_2, CeO_x/CoO_x and Co_3O_4/CeO_2) not only exhibit excellent catalytic activity for OER [26–28], but also can achieve total water decomposition and pollutant oxidation in a wide pH range [29–31]. However, there are few studies on the selective electrocatalytic conversion of biomass derivatives.

Based on the above problems, in this work, we design and prepare a cobalt hydroxide-cerium dioxide composite catalyst $Co(OH)_2$-CeO_2 for selective electrocatalytic conversion of HMF coupling hydrogen production under neutral condition. The relationships among catalyst composition, solution chemistry, applied potential, activity of HMF electrooxidation and product selectivity are studied by electrochemical test methods and in situ electrochemical Raman spectroscopy. Under the neutral condition of pH 7, $Co(OH)_2$-CeO_2 achieves selective two-electron electrocatalytic conversion of HMF to HMFCA (selectivity of 89.4%) at 1.4 V. In situ Raman reveal that the evolution of active species between CoOOH and CoO_2 is the key factor for the selective electrooxidation of HMF. In addition, we study the effect of HMF selective oxidation on cathodic hydrogen production at different potential, it is found that HMF mild oxidation to HMFCA is more conducive to hydrogen production than deep oxidation. This new system of selective electrocatalytic conversion of biomass derivatives coupled with hydrogen production realizes the simultaneous production of value-added chemicals and clean energy, which is of great significance in responding to the energy crisis and realizing the vision of carbon neutrality.

2. Experimental

2.1. Synthesis of the Catalyst of $Co(OH)_2$-CeO_2

Firstly, the commercial carbon paper was cut into 1.0 cm × 3.0 cm. Before using, the carbon paper was ultrasonicated in 3 M HCl for 30 min, deionized water for 30 min, acetone for 30 min, deionized water for 30 min, and the surface oxide layer was taken out. Finally, the carbon paper was soaked in concentrated sulfuric acid for 2 h, washed with deionized water, and dried overnight in an oven at 60 °C to obtain a hydrophilic carbon paper substrate CP.

The required $Co(OH)_2$-CeO_2 catalyst was prepared by electrodeposition in a three-electrode system. The treated CP was used as the working electrode, the saturated calomel electrode SCE was used as the reference electrode, the Pt sheet was used as the counter electrode, and the electrolyte was a 30 mL mixed solution of 0.09 M $Co(NO_3)_2$ and 0.01 M $Ce(NO_3)_2$. Firstly, the working electrode was treated with an anodic current density of 20 mA cm^{-2} for 600 s, and the NO^{3-} ion was inserted into the carbon paper substrate. Then, the working electrode was deposited with a reduction current density of − 20 mA cm^{-2} for 300 s. After the deposition, the working electrode was washed with deionized water and dried overnight in an oven at 60 °C to obtain $Co(OH)_2$-CeO_2. The preparation of CeO_2 and $Co(OH)_2$ is the same as the above process, but the electrolyte is replaced by 0.1 M $Co(OH)_2$ and 0.1 M $Ce(NO_3)_2$, respectively. The electrode $Co(OH)_2$-CeO_2 with the ratio of $Co(OH)_2$ to CeO_2 of 5:1 and 15:1 were prepared with the same procedure as $Co(OH)_2$-CeO_2 with the ratio of $Co(OH)_2$ to CeO_2 of 9:1, except that the concentration of 0.083 M $Co(NO_3)_2$ and 0.017 M $Ce(NO_3)_2$ for $Co(OH)_2$-CeO_2 (5:1), and 0.094 M $Co(NO_3)_2$ and 0.006 M $Ce(NO_3)_2$ for $Co(OH)_2$-CeO_2 (15:1), respectively.

2.2. Characterization of catalyst

The morphology of the samples was characterized by field emission scanning electron microscopy (FE-SEM, Hitachi S-4800, Japan) and high resolution transmission electron microscopy (HR-TEM, 2100, JEOL, Japan). The crystal structure of the sample was observed with X-ray diffraction (XRD, D8 Focus X-ray diffractometer, Bruker, Germany, Cu target: λ = 1.540598 Å tube voltage 40 kV). X-ray photoelectron spectroscopy (XPS, AXIS Ultra DLD, Kratos Analytical Ltd, UK, ultra-high vacuum < 10^{-8} torr, Mg target, 150 W) was used to determine the chemical composition and valence changes of the materials. Raman spectra were measured by Renishaw 's inVia Reflex confocal Raman microscopy spectrometer. The 532 nm wavelength semiconductor laser is used as the excitation light source, which is focused by a 50-fold long focal lens. All spectra are corrected by a silicon wafer at 520 cm^{-1}.

2.3. Electrochemical measurement

At room temperature, the electrocatalytic oxidation performance and electrolysis performance of HMF were tested by three-electrode system using Chenhua workstation CHI660C (CH Instruments Inc., USA). $Co(OH)_2$-CeO_2 was used as the working electrode, the working area was 1 cm^2, Ag/AgCl was used as the reference electrode, Pt wire was used as the counter electrode, and the electrolyte was 0.1 M PBS solution containing 10 mM HMF with pH of 7 or 1 M NaOH with pH of 8 or 10. Linear sweep voltammetry (LSV), chronoamperometry (I-t), electrochemical impedance spectroscopy (EIS), cyclic voltammetry (CV) were used to study the current density and electrochemical stability of the sample electrode. The measured potential was expressed by the Nernst equation converted into a reversible hydrogen electrode potential:

$$E_{RHE} = E_{Ag/AgCl} + 0.059 \times pH + 0.197\ V$$

In order to qualitatively and quantitatively analyze HMF and its oxidation products, HPLC (Extended C18 column, 4.6 mm × 1150 mm, UV detector wavelength set at 261 nm) was used to detect the solution substances during the constant voltage test. Mobile phase: 90% ammonium formate: 10% methanol, mobile phase: 1 mL min^{-1}. During the constant voltage test, 10 μL of the electrolysis process solution was diluted with 490 μL of water each time, and 10 μL of the diluted solution was injected into the HPLC instrument for testing. The standard solution of the known concentration of the reactants and products is configured to make the corresponding standard curve, and the qualitative and quantitative analysis of the substances in the constant voltage test process is carried out. The qualitative and quantitative analysis of cathode

hydrogen was carried out using a gas chromatograph equipped with a thermal conductivity detector (TCD) (DC7900, Shanghai Tianmei). The off-line sampling method was used to sample 1 mL each time at the cathode headspace position into gas chromatography. The conversion of HMF and the yield and selectivity of the product are calculated according to the formula below:

$$\text{HMF conversion } (\%) = \frac{\text{mol of HMF consumed}}{\text{mol of initial HMF}} \times 100 \quad \%$$

$$\text{Yield of product } (\%) = \frac{\text{mol of products formed}}{\text{mol of initial HMF}} \times 100 \quad \%$$

$$\text{Selectivity of product } (\%) = \frac{\text{mol of products formed}}{\text{mol of all products formed}} \times 100 \quad \%$$

The energy consumption (Ec) during hydrogen production were calculated according to the following equations:

$$Ec = \frac{Ucell \times I \times t}{3600}$$

where Ucell is the applied potential (V), I is the circuit current (A), t is the electrolysis time (s).

2.4. In situ electrochemical Raman spectroscopic measurements

The in situ electrochemical Raman spectroscopic measurements were carried out on a confocal Raman microscope (Invia Reflex, Renishaw, UK). The applied potential was tuned by a CHI660 electrochemical workstation. All Raman spectra were acquired with a home-made spectra-electrochemical quartz cell. It was coated with the as-prepared catalyst and served as the working electrode. An Ag/AgCl electrode served as reference electrode and a Pt wire served as counter electrode. The calibration was conducted with a silicon wafer at a wavenumber of 520 cm^{-1}. A semiconductor laser with a wavelength of 532 nm was used as the excitation light source. It was focused by 50 times long focal lens to vertically illuminate the surface of the working electrode. The spectra after the chronoamperometric tests were collected in 0.1 M PBS solution with pH 7 or adjusted concentration NaOH solution with pH 10 containing 10 mM HMF. The applied time was 5 min. The applied potential was in the range from 1.10 to 1.60 V

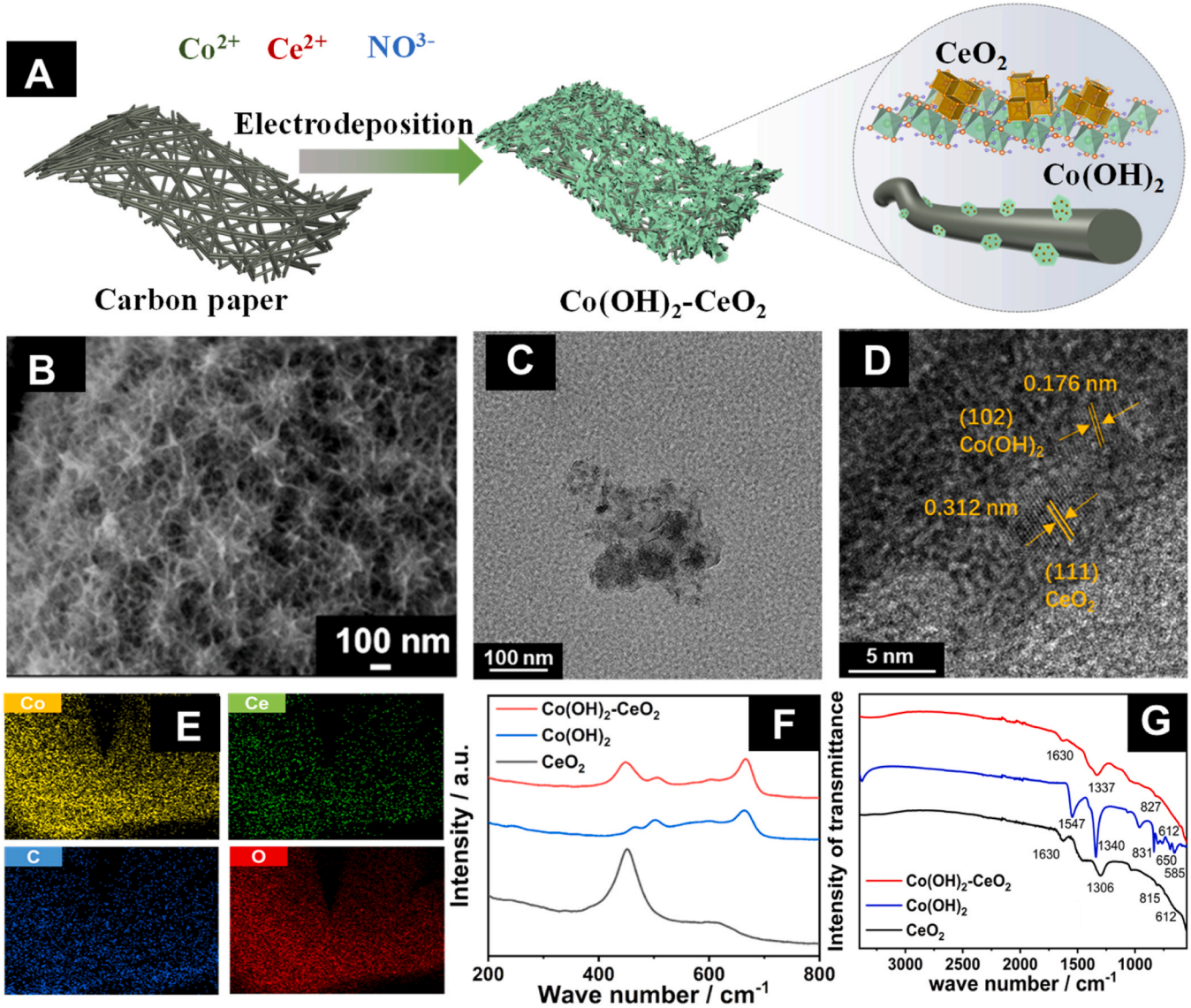

Fig. 1. Schematic illustration for synthesis of $Co(OH)_2$-CeO_2 electrode(A). High magnification SEM spectra of $Co(OH)_2$-CeO_2 electrode (B). TEM spectra of $Co(OH)_2$-CeO_2 with low (C)and high magnification (D). EDS mapping of $Co(OH)_2$-CeO_2 electrode (E). Raman spectra (F) and infrared spectra (G) of $Co(OH)_2$ electrode, CeO_2 electrode and $Co(OH)_2$-CeO_2 electrode.

with an interval of 0.1 V.

3. Results and discussion

3.1. Characterization of $Co(OH)_2$-CeO_2

Firstly, $Co(OH)_2$, CeO_2 and $Co(OH)_2$-CeO_2 electrodes are prepared by

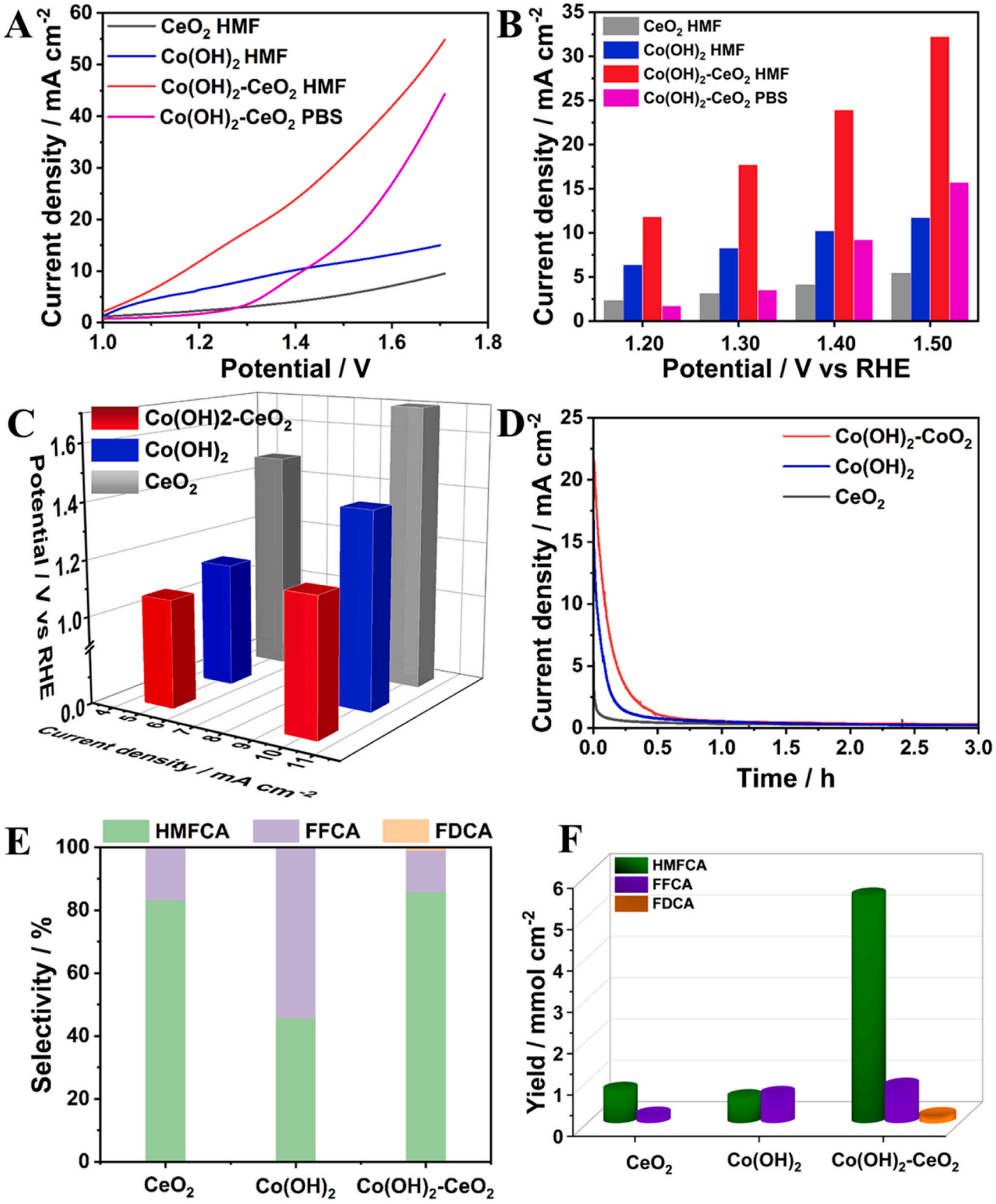

Fig. 2. LSV test curves (A) of CeO_2, $Co(OH)_2$, and $Co(OH)_2$-CeO_2 electrodes in 0.1 M PBS solution containing 10 mM HMF. Comparison of current density of different electrodes at the same potential (B). Comparison of the potential of CeO_2, $Co(OH)_2$, and $Co(OH)_2$-CeO_2 at 5 and 10 mA cm^{-2} (C). The electrolysis I-t curves (D), product selectivity distribution (E), and product yield distribution (F) of $Co(OH)_2$, CeO_2, and $Co(OH)_2$-CeO_2 in 0.1 M PBS solution containing 10 mM HMF at 1.3 V.

simple electrodeposition method in different precursors. The schematic illustration of $Co(OH)_2$-CeO_2 is shown in Fig. 1A. The SEM results are shown in Fig. 1 and Fig. S1. In the SEM with high magnification of $Co(OH)_2$-CeO_2 (Fig. 1B), it can be seen that $Co(OH)_2$-CeO_2 is uniformly distributed on the carbon paper substrate in the form of nanosheets. According to the SEM images of the three catalysts with low magnification (Fig. S1), where $Co(OH)_2$ exhibits a nanosheets structure, CeO_2 exhibits a nanosphere structure, and the $Co(OH)_2$-CeO_2 composite retains a nanosheets structure similar to $Co(OH)_2$. Figs. 1C and 1D shows the TEM images of $Co(OH)_2$-CeO_2 electrode. The low-magnification TEM reveals that the composite still maintains the morphology of the sheet. HR-TEM shows lattice spacing of 0.312 nm and 0.167 nm, corresponding to CeO_2(111) and $Co(OH)_2$(102) crystal planes, respectively, indicating the successful preparation of $Co(OH)_2$-CeO_2 composite electrode [32,33]. The element mapping further shows the uniform distribution of Co, Ce and O on the carbon substrate (Fig. 1E). The energy dispersive spectra shown in Fig. S1D demonstrate that the Co content in the material is much higher than that of Ce.

In addition, the prepared CeO_2, $Co(OH)_2$ and $Co(OH)_2$-CeO_2 materials were characterized by Raman and infrared spectroscopy to study the composition of the materials. In the Raman spectrum (Fig. 1F), the CeO_2 material has an obvious characteristic peak at 451 cm^{-1}, corresponding to the asymmetric breathing mode of oxygen atoms around cerium ions in CeO_2. In $Co(OH)_2$, the characteristic peaks attributed to $Co(OH)_2$ appeared at 250 cm^{-1} and 506 cm^{-1}, and the characteristic peaks corresponding to CoOOH appeared at 463 cm^{-1} and 606 cm^{-1}, and the characteristic peaks attributed to Co_3O_4 appeared at 667 cm^{-1}, indicating that the prepared $Co(OH)_2$ was oxidized and existed in the form of coexistence of various valence Co species. In the $Co(OH)_2$-CeO_2 material, the characteristic peaks of CeO_2 and various valence Co species coexist, indicating the successful preparation of cobalt hydroxide-cerium oxide composites [34,35]. In the corresponding infrared spectra (Fig. 1G), the low frequency region below 1000 cm^{-1} wavenumber in CeO_2 is observed. The transmission peaks, including 612 cm^{-1} and 815 cm^{-1}, belong to the characteristic peaks of Ce-O stretching mode, indicating the formation of CeO_2 structure. In $Co(OH)_2$, the transmission peaks at 585 cm^{-1}, 650 cm^{-1}, and 831 cm^{-1} correspond to the vibration peaks of Co-O, O-Co-O, and Co-O-Co. The peak at 3370 cm^{-1} in the higher frequency region is caused by the OH stretching vibration of the hydroxyl functional group on the surface, indicating the formation of $Co(OH)_2$ structure. In $Co(OH)_2$-CeO_2, a characteristic peak corresponding to M-O (M = Co, Ce) appeared at 827 cm^{-1}, which was located between the metal-oxygen peaks of $Co(OH)_2$ and CeO_2, indicating the formation of the composite catalyst [36,37].

3.2. Selective electrocatalytic conversion performance of HMF on $Co(OH)_2$-CeO_2

Then, the electrochemical performance of $Co(OH)_2$, CeO_2 and $Co(OH)_2$-CeO_2 electrode for elctrocatalytic conversion of HMF is characterized in neutral condition. The liner sweep voltammetry (LSV) curves are shown in Fig. 2A. In 0.1 M PBS solution, the $Co(OH)_2$-CeO_2 composite electrode shows a current rise near 1.30 V, which is attributed to the oxidation of Co^{2+} species. When the potential continues to rise to 1.50 V, obvious bubbles resulted from water oxidation appear on the anode catalyst. When 10 mM HMF was added, the current density begins to increase gradually at 1.0 V, and an obvious oxidation peak appeared at 1.30 V. The intensity was much higher than that of 0.1 M PBS system, which could be attributed to the oxidation of HMF, indicating that the oxidation potential of HMF was significantly lower than that of water. We also compare the current density of $CeoO_2$, $Co(OH)_2$, and $Co(OH)_2$-CeO_2 electrodes in 0.1 M PBS solution containing 10 mM HMF at the same potential, and the current density of $Co(OH)_2$-CeO_2 electrode in 0.1 M PBS solution (Fig. 2B). It can be seen that when the $Co(OH)_2$-CeO_2 electrode is tested in the system with 10 mM HMF, the current densities after adding HMF at 1.20 V, 1.30 V, 1.40 V and 1.50 V are 12, 17, 23, 32 mA cm^{-2}, respectively, which is about 2–6 times of the current density in the pure 0.1 M PBS system, indicating that HMF oxidation is thermodynamically more favorable than water oxidation, and the addition of HMF effectively promotes the current density. In addition, it is found that $Co(OH)_2$ has an onset potential of about 1.0 V close to that of $Co(OH)_2$-CeO_2, and the onset potential of CeO_2 is about 1.32 V, which is much lower than that of the former two. And in the whole potential range, the current density of the $Co(OH)_2$-CeO_2 composite electrode is higher than that of the $Co(OH)_2$ electrode and the CeO_2 electrode. We also compared the needed potential of the prepared three electrodes at 5 and 10 mA cm^{-2} current densities, as shown in Fig. 2C. At 5 mA cm^{-2}, the potential of $Co(OH)_2$-CeO_2 is 1.07 V, which is lower than that of $Co(OH)_2$ (1.13 V) and CeO_2 (1.48 V). At 10 mA cm^{-2}, $Co(OH)_2$-CeO_2 also exhibit lower potential (1.17 V) than $Co(OH)_2$ (1.39 V) and CeO_2 (1.7 V), indicating that the composite catalyst effectively improves the HMF electrooxidation performance.

Through electrochemical LSV, we have confirmed that the oxidation thermodynamics of HMF is better than that of water under neutral conditions, and the activity of $Co(OH)_2$-CeO_2 composite electrode for HMF oxidation is higher than that of $Co(OH)_2$ and CeO_2. We further use constant potential electrolysis to study the performance of three prepared electrodes for electrocatalytic conversion of HMF. According to the test results of the LSV polarization curve, an obvious oxidation peak appeared at a potential of 1.3 V, so we selected a potential of 1.3 V for electrolysis. The electrochemical I-t curve is shown in Fig. 2D. It can be seen that the HMF oxidation current density on the electrode $Co(OH)_2$-CeO_2 is significantly higher than that of $Co(OH)_2$ and CeO_2, and the HMF oxidation current density on the $Co(OH)_2$ electrode is higher than that of CeO_2, which is consistent with the LSV polarization curve. The products of electrolysis are detected by high performance liquid chromatography (HPLC) (Fig. S2A-S2C), it can be seen from the HPLC spectra that the strength of HMFCA and FFCA on CeO_2 and $Co(OH)_2$ is low, while the strength of HMFCA on $Co(OH)_2$-CeO_2 is much higher than that on CeO_2 and $Co(OH)_2$, and a small amount of FDCA is generated. Corresponding product selectivity results are shown in Fig. 2E. It can be seen that the product HMFCA is dominated by nearly 83% selectivity on the CeO_2 electrode, and the FFCA selectivity is about 17%. On the $Co(OH)_2$ electrode, the product HMFCA selectivity decreases to about 46%, while the FFCA selectivity is about 54%. On the $Co(OH)_2$-CeO_2 electrode, the HMFCA selectivity is 86%, which is close to CeO_2. The FFCA selectivity is about 12% accompanying by a small amount of FDCA formation with selectivity of 2%. The corresponding product yield results are shown in Fig. 2F. It can be seen that the concentration of HMFCA and FFCA on CeO_2 and $Co(OH)_2$ is below 1 mmol cm^{-2}, while the concentration of HMFCA on $Co(OH)_2$-CeO_2 is 5.5 mmol cm^{-2}, the concentration of FFCA is 0.9 mmol cm^{-2}, and the concentration of FDCA is 0.18 mmol cm^{-2}. These demonstrate that HMF on CeO_2 electrode is prone to generate HMFCA through two-electron oxidation of aldehyde group, and the oxidation of both alcohol hydroxyl group and aldehyde group can occur on $Co(OH)_2$, but both CeO_2 and $Co(OH)_2$ electrodes have the problem of low yield. The high yield of HMFCA on the $Co(OH)_2$-CeO_2 electrode indicates that the combination of the two metal oxide species effectively promotes the activity of HMF and the high selectivity of the product HMFCA.

The proportion adjustment of the active component has a great influence on the overall performance of the composite electrode. So we prepared catalysts with the ratio of $Co(OH)_2$ to CeO_2 of 5:1 and 15:1, and carried out LSV test and electrolysis test at 1.3 V , and studied the products distribution (Fig. S3). The results show that the $Co(OH)_2$-CeO_2 electrode with a theoretical ratio of 9:1 exhibits the best onset potential and HMF electrooxidation activity. From the perspective of HMFCA selectivity, compared with the selectivity of 53.6% and 79.8% exhibited by $Co(OH)_2$-CeO_2 (5:1) and $Co(OH)_2$-CeO_2 (15:1) electrodes, the $Co(OH)_2$-CeO_2 (9:1) electrode exhibits the best selectivity, indicating that the proper incorporation of CeO_2 can effectively improve the activity of

HMF electrooxidation and the selectivity of mild oxidation product HMFCA.

By comparing the electrocatalytic oxidation performance of HMF on the three materials, we have determined that the $Co(OH)_2$-CeO_2 composite has excellent performance in HMF electrocatalytic oxidation activity and achieves mild oxidation to HMFCA under neutral condition. Therefore, we further explored the effect of the pH value of the electrolyte on the selective electrocatalytic conversion of HMF. The biomass derivative 5-hydroxymethylfurfural is composed of a hydroxyl group and an aldehyde group attached to the furan ring, so the oxidation degree of HMF depends on the oxidation behavior of hydroxyl group and aldehyde group. The intermediate product HMFCA of HMF oxidation is composed of a furan ring with an alcohol hydroxyl group and a carboxyl group, and FFCA is composed of an aldehyde group and a carboxyl group on the furan ring. Therefore, we chose HMFCA and FFCA as substrates for electrochemical tests to study the oxidation behavior of alcohol hydroxyl groups and aldehyde groups under different pH conditions.

The open circuit potential-time (OCPT) curves of HMFCA and FFCA under different pH conditions are shown in Fig. 3 A. At pH 7, the open circuit potential of FFCA (1.028 V) is slightly lower than that of HMFCA (1.037 V), indicating that the aldehyde group is more prone to oxidation. When pH was 8, the open circuit potential of HMFCA and FFCA

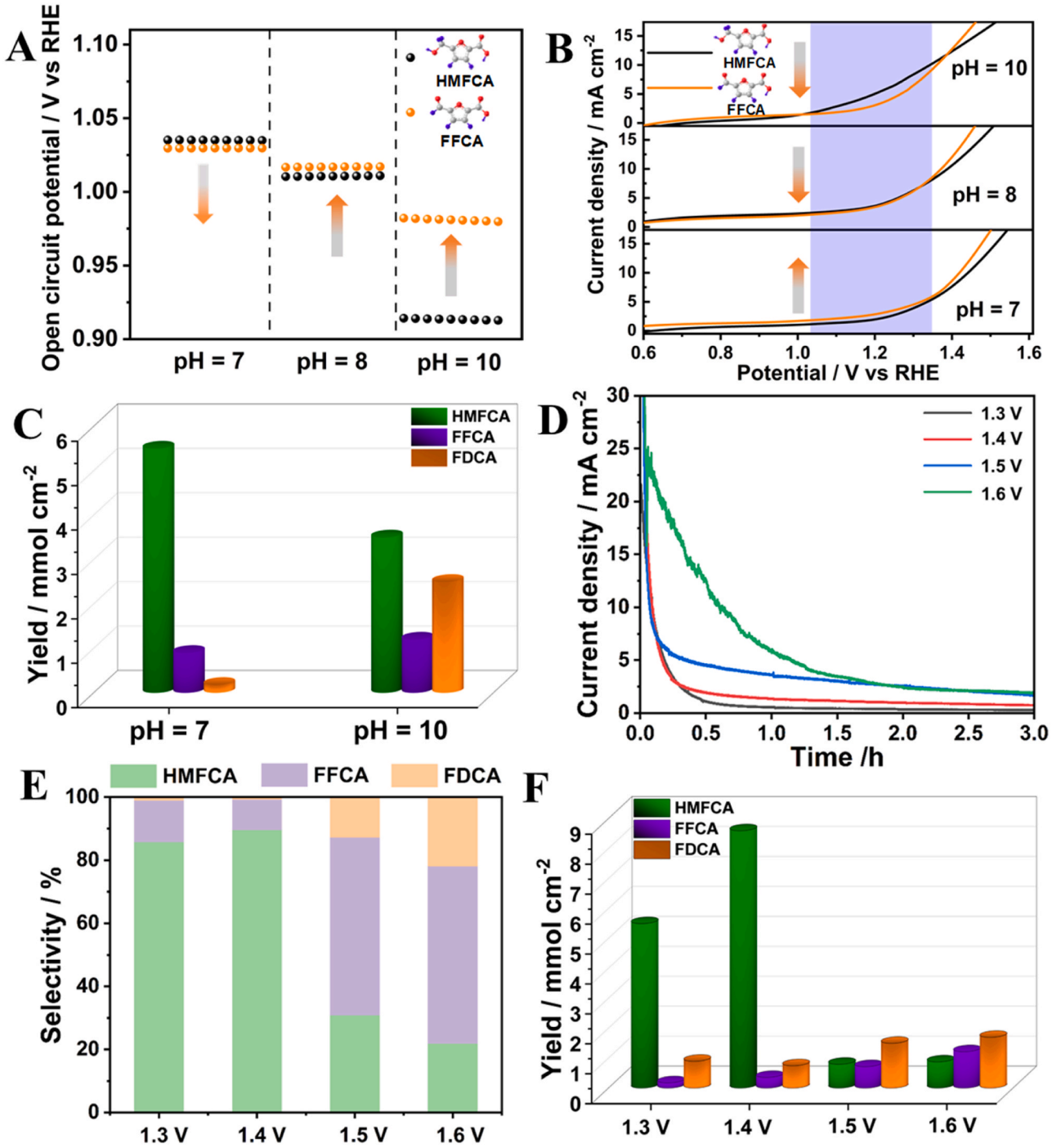

Fig. 3. OCPT measurements (A) and LSV curves (B) of $Co(OH)_2$-CeO_2 in 0.01 M HMFCA and 0.01 M FFCA at pH 7, pH 8, pH 10. Yield distribution (C) of $Co(OH)_2$-CeO_2 at pH 7 and pH 10. The electrolysis I-t curves of $Co(OH)_2$-CeO_2 in 0.1 M PBS solution containing 10 mM HMF at different potential (D). The selectivity distribution (E) and yield distribution (F) of products at different potentials.

decreased to a certain extent, and the open circuit potential of HMFCA was slightly lower than that of FFCA, indicating that the oxidation of alcohol hydroxyl groups was more likely to occur than the oxidation of aldehyde groups. When the pH was further increased to 10, the open circuit potential of HMFCA was about 60 mV lower than that of FFCA, indicating that the increase of pH has a greater oxidation effect on the oxidation of alcohol hydroxyl groups, and the oxidation of alcohol hydroxyl groups was better than that of aldehyde groups. We further studied the oxidation of alcohol hydroxyl and aldehyde groups at different pH by electrochemical polarization curves of HMFCA and FFCA. Under different pH conditions, the results of linear sweep voltammetry curves are shown in Fig. 3B. At pH 7, It can be seen that the oxidation current of FFCA is higher than that of HMFCA in the selected oxidation potential range, indicating that the oxidation of aldehyde group is better than that of alcohol hydroxyl group at pH 7. In the polarization curves of the two substances at pH 8, the oxidation curves of HMFCA and FFCA almost coincide before 1.35 V, indicating that the alcohol hydroxyl group and the aldehyde group have similar oxidation kinetics under this condition. With the further increase of pH, the oxidation current of HMFCA is higher than that of FFCA between 1.0 and 1.4 V, indicating that the oxidation of alcohol hydroxyl group is better than that of aldehyde group. In the two electrochemical experiments, the open circuit potential and oxidation current of FFCA change little with the increase of pH, while the open circuit potential of HMFCA decreases significantly with the increase of pH, and the oxidation current increases significantly at lower potential, indicating that pH has a greater effect on the oxidation of alcohol hydroxyl groups. The oxidation of alcohol hydroxyl groups is significantly inhibited at low pH, while the oxidation of aldehyde groups does not change much. Therefore, the product is mainly HMFCA at low pH, while FFCA and FDCA tend to be generated at high pH theoretically, and the controllable products distribution of selective electrocatalytic conversion of HMF could be achieved by adjusting value of pH. So we conduct electrolysis tests in a solution containing 10 mM HMF at pH 10 to study the distribution of the product. The electrolysis potential is selected at 1.3 V. Fig. S4A is the I-t curve in HMF solution with pH of 10 at 1.3 V voltage. It can be seen that the overall current is slightly higher than the current under the condition of pH 7 solution. Fig. S4B is the corresponding Charge-t curve, and the transferred charge is about 34 C. The results of HPLC are shown in Fig. S4C. Different from the product dominated by HMFCA under low pH conditions, the yield of FFCA and FDCA increase significantly at pH 10. The yield distribution is shown in Fig. 3C, at pH 10, the yield of FDCA increases significantly to 2.5 mmol cm^{-2}, the yield of FFCA increases slightly to 1.2 mmol cm^{-2}, and the yield of HMFCA decreases slightly to 3.4 mmol cm^{-2}. This also indicates that low pH is conductive to mild oxidation of HMF to HMFCA, and the increase of pH is conducive to the oxidation of alcohol hydroxyl groups, resulting in high yield of FFCA and FDCA, which is consistent with the results revealed by electrochemical experiments.

In addition to the pH value, we also study the effect of different potentials on the selective electrocatalytic conversion of HMF under neutral conditions on $Co(OH)_2$-CeO_2. Fig. 3D is the I-t curve of electrolysis in 0.1 M PBS solution containing 10 mM HMF at 1.3 V, 1.4 V, 1.5 V and 1.6 V. It can be seen from the figure that the electrolysis current increases with the increase of potential, and the current at 1.4 V increases to a certain extent compared with the current at 1.3 V, while the current at 1.5 V and 1.6 V increases significantly. This is due to the obvious water oxidation with the increase of potential, resulting in a significant promotion in the overall current. The HPLC spectra at different potentials are shown in Fig. S5A-S5C, and the selectivity of the product at four potentials is shown in Fig. 3E. It can be seen that the selectivity of HMFCA at 1.4 V has a certain degree of improvement, reaching 89.4%. The selectivity of HMFCA, FFCA and FDCA at 1.5 V is 30.1%, 56.3% and 12.6%, respectively. The selectivity of HMFCA decreases significantly, and the selectivity of FFCA and FDCA is significantly higher than that at 1.3 V and 1.4 V. At 1.6 V, the selectivity of HMFCA further decreases, the selectivity of HMFCA, FFCA and FDCA is 21.9%, 56.3% and 21.8%, respectively. These indicate that HMF undergoes the two-electron oxidation of aldehyde group to HMFCA at low potential, and the alcohol hydroxyl group is oxidized with the increase of potential so that FFCA and FDCA through four-electrons and six-electrons oxidation generate simultaneously. The corresponding product yield distribution at different potentials is shown in Fig. 3F. The yield of HMFCA is 8.5 mmol cm^{-2} at 1.4 V, which maximizes the yield of HMFCA. Compared with other catalysts (Table S1, Supporting Information), the $Co(OH)_2$-CeO_2 catalyst exhibits superior performance of selective electrocatalytic conversion of HMF into HMFCA under neutral condition, and even exceeds some results reported under alkaline condition.

Considering the actual industrial application scenarios, we designed a flow cell with a reaction area of 6×6 cm^2, and integrated the 3×3 cm^2 $Co(OH)_2$-CeO_2 electrode into the flow cell to study its performance for HMF mild electrooxidation coupling hydrogen production [38–41]. The photograph of flow cell and corresponding performance are shown in Fig. S6. Firstly, the LSV test of the electrode was carried out. It can be seen that the oxidation current density of the system in the flow cell was greatly increased after 1.2 V. The current density was close to 2 times that of the H-type cell at 1.4 V, and the current density reached 100 m A cm^{-2} at 1.7 V. Then, we performed 6 cycles and large volume I-t tests in a flow cell, and found that the electrolysis time was significantly shortened compared to the H-type cell, and the selectivity and yield of HMFCA were above 93% and 9.2 mM in 6 cycles and long time electrolysis. These indicate that the prepared $Co(OH)_2$-CeO_2 electrode also has good electrocatalytic performance and good stability of HMF oxidation in the flow cell and has industrial application potential.

3.3. *Promoted hydrogen production coupled with selective electrocatalytic conversion of HMF*

While measuring the selective conversion of anodic HMF, we also detect the production of cathodic hydrogen. We first compare the electrochemical polarization curves in 0.1 M PBS solution with and without 10 mM HMF at 1.3 V (Fig. 4A). The current density in pure PBS solution is maintained at 2.5 mA cm^{-2}. After adding HMF, the initial current density increases to 20 mA cm^{-2}, which is much higher than that of PBS solution system. After 1 h of electrolysis, the transferred charge in the HMF system is about 13 C, and the current density is reduced to about 1 mA cm^{-2}. We also detected the hydrogen production of the cathode. The results are shown in Fig. 4B. The hydrogen production rate in the HMF system was 66.28 μmol cm^{-2} h^{-1}, which was 7.49 times that of the PBS system. These demonstrate that HMF selective oxidation can replace the oxygen evolution reaction and effectively promote the production of hydrogen.

In addition, we use the same concentration of HMFCA in anode chamber to study the coupled cathodic hydrogen production under different potential, and the results are shown in Fig. 4C-4D. At 1.4 V (Fig. 4C), the conversion of HMF was 96%, while the conversion of HMFCA was only 3.8%. At the same time, the corresponding hydrogen production rate of HMF oxidation system was 114.39 μmol cm^{-2} h^{-1}, which was 4.1 times that of HMFCA oxidation system, and about 74.1% of hydrogen in HMFCA oxidation system came from water oxidation. This indicates that the mild oxidation of HMF promotes hydrogen production more than deep oxidation. When the potential further increases to 1.6 V (Fig. 4D), the conversion rate of HMF is only about 41% due to the intensification of competitive water oxidation reaction. The cathodic hydrogen production corresponding to the HMF oxidation system is still higher than that of the HMFCA oxidation system. Combined with the conversion of HMF and the cathodic hydrogen production rate, we believe that 1.4 V is a better electrolysis potential for anodic high-efficiency mild oxidation coupled with cathodic hydrogen production.

At present, industrialized green hydrogen production is usually carried out at high potential and high current density, and the energy

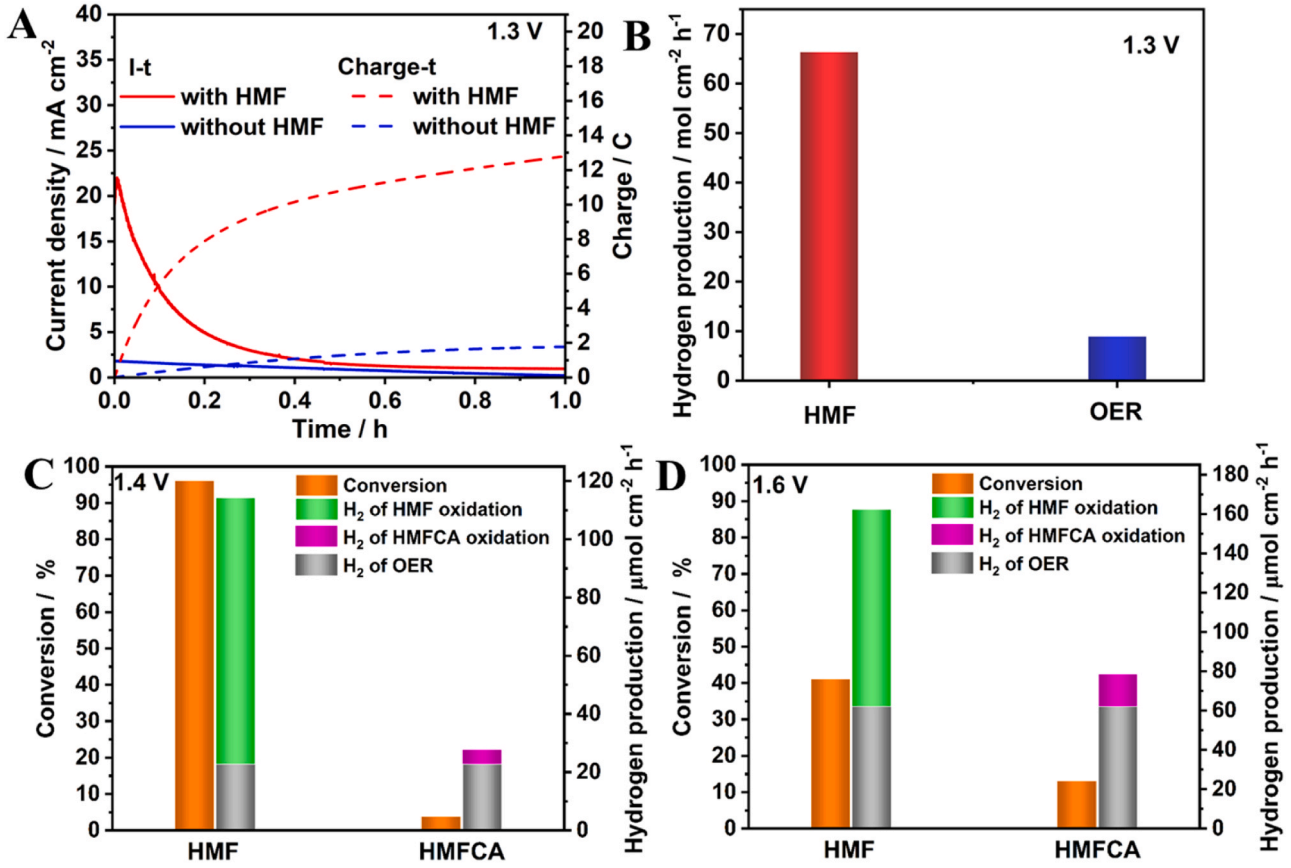

Fig. 4. I-t and Charge-t curves of $Co(OH)_2$-CeO_2 in 0.1 PBS with and without 0.01 M HMF at pH 7 under 1.3 V (A). Cathodic hydrogen production with anodic chamber full of 0.1 M PBS with and without 0.01 M HMF at pH 7 under 1.3 V (B). The conversion of HMF and HMFCA as reactants and the amount of hydrogen produced on the cathode at 1.4 V (C) and 1.6 V (D).

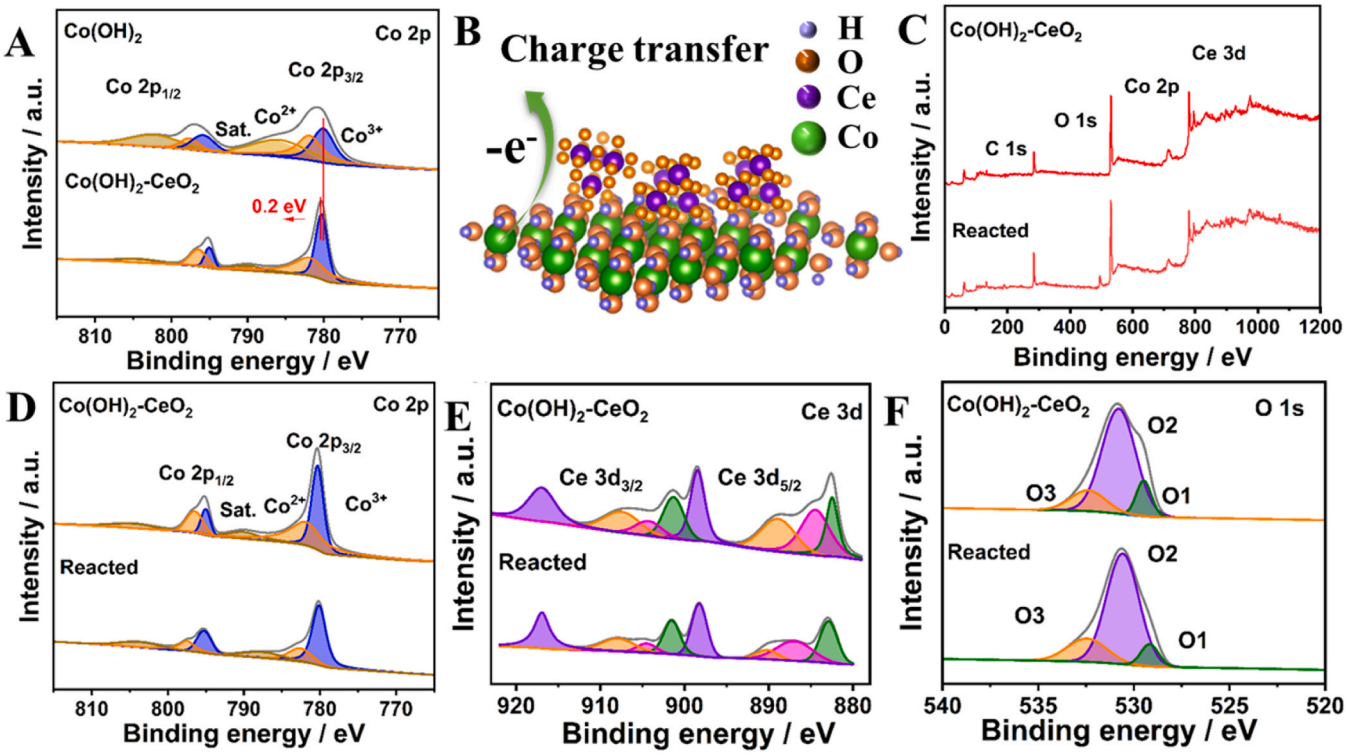

Fig. 5. High resolution XPS spectra of Co 2p (A) of $Co(OH)_2$ and $Co(OH)_2$-CeO_2 catalyst. Schematic illustration of electron transfer of $Co(OH)_2$-CeO_2 (B), Full scan (C) and high resolution XPS spectra of Co 2p (D), Ce 3d (E) and O 1 s (F) of $Co(OH)_2$-CeO_2 catalyst before and after 1.4 V electrolysis.

consumption is about 5 kWh $Nm^{-3}H_2$. In the HMF mild oxidation coupled hydrogen production system, when the HMFCA yield is maximized at a potential of 1.4 V, the hydrogen production energy consumption of the system is calculated to be 3.35 kWh $Nm^{-3}H_2$, which is 33% lower than that of electrolytic hydrogen production. At the same time, the cost change due to reduced energy consumption has been reduced from 4.3 \$ kg^{-1} to 3.2 \$ kg^{-1}. Considering the economic benefits and commercial application prospect of the paired electrolysis, we study the TEA of our work to estimate the economic benefits on the basis of related literature on the TEA in related electrolysis process [42–44], and the detailed process could be seen in Supplementary note 1. The calculated minimum price of coproduction of HMFCA and H_2 based on paired electrolysis process is 7.46 \$ (per kg HMFCA and 0.014 kg H_2), which is much lower than the market price of HMFCA through chemical or biosynthesis process (1380 \$ kg^{-1}), and a certain amount of hydrogen is simultaneously produced, showing great economic benefits. Therefore, it is of great significance in reducing energy consumption and cost of hydrogen production through HMF mild oxidation coupling hydrogen production [45–47].

3.4. Reaction mechanism of selective electrocatalytic conversion of HMF

To determine the effect of CeO_2 addition on the electrocatalytic performance of $Co(OH)_2$, we first use XPS to analyze the electronic structure of Co element in $Co(OH)_2$ and Co $(OH)_2$-CeO_2 catalysts. In the Co XPS spectrum of $Co(OH)_2$ (Fig. 5A), the Co $2p_{3/2}$ peaks at 780.1 eV and 781.9 eV are assigned to Co^{3+} and Co^{2+}. After the incorporation of CeO_2, there is a positive shift of 0.2 eV in Co $2p_{3/2}$ $Co(OH)_2$-CeO_2 XPS spectrum, where two peaks appear at 780.3 eV and 782.1 eV correspond to Co^{3+} and Co^{2+}, respectively. Furthermore, the ratio of Co^{3+}/Co^{2+} changes from 0.95 to 1.15 after incorporation of CeO_2, indicating the formation of more Co^{3+} species due to the adding of CeO_2 and the electron transfer from $Co(OH)_2$ to CeO_2, and the schematic figure is shown in Fig. 5B. Based on the XPS results, the molar ratio of Ce to Co is 1:9.5 (Table S2), which is close to the theoretical value of 1:9 calculated by the synthetic scheme. In order to explore the species changes of Co $(OH)_2$-CeO_2 electrode in the process of HMF selective electrooxidation, we carry out XPS test of $Co(OH)_2$-CeO_2 electrode before and after 1.4 V electrolysis. Fig. 5C is the full spectrum of $Co(OH)_2$-CeO_2 electrode before and after electrolysis. It can be seen that the electrode contains O, Co and Ce elements. In the XPS map of Co element after electrolysis (Fig. 5D), Co^{2+} and Co^{3+} coexist and locate at 780.2 eV and 782.6 eV, respectively. Compared with the peak position of Co element before electrolysis, there is no significant change, but the ratio of Co^{3+}/Co^{2+} increases from 1.15 to 2.94, indicating that Co^{3+} species increase and there is a conversion of Co^{2+} to Co^{3+}. In the XPS spectrum of Ce element (Fig. 5E), the peaks corresponding to Ce^{4+} in Ce $3d_{5/2}$ appear at 882.4, 888.9 and 898.6 eV before electrolysis, the characteristic peak corresponding to Ce^{3+} appears at 884.5 eV, the peaks corresponding to Ce^{4+} in Ce $3d_{3/2}$ appear at 901.4, 907.4 and 916.9 eV, and the characteristic peak corresponding to Ce^{3+} appears at 904.2 eV, indicating the successful synthesis of CeO_2 in $Co(OH)_2$-CeO_2 electrode [54]. However, the peak positions of Ce element do not change greatly after electrolysis. In the XPS spectrum of the O element shown in Fig. 5F, three peaks at 529.5, 530.8, and 532.4 eV are assigned to the metal-oxygen M-O-M bond (O1), low-coordination oxygen defect (O2), and adsorption peak (O3), respectively [52]. The peak positions of O1, O2, and O3 do not change much before and after electrolysis, but the content of low-coordination defect oxygen in O2 increases to a certain extent. The proportion of metal-oxygen M-O-M changed from 0.11 to 0.08 after the reaction. Combined with the change of Co^{3+} content in Co, it shows that the oxide species of Co with higher valence is generated.

In addition, we use electrochemical in situ Raman spectroscopy to monitor the species evolution of $Co(OH)_2$-CeO_2 electrode under electrolysis at different potentials to analyze its active species in the selective electrocatalytic conversion of HMF. The results are shown in Fig. 6. Fig. 6A is the in situ Raman spectrum of $Co(OH)_2$-CeO_2 electrode under electrolysis from 1.1 V to 1.6 V. At 1.1 V, the characteristic peaks corresponding to CoOOH and $Co(OH)_2$ appear at 363 and 523 cm^{-1} [53]. When increasing potential to 1.2 V, the position and intensity of Raman

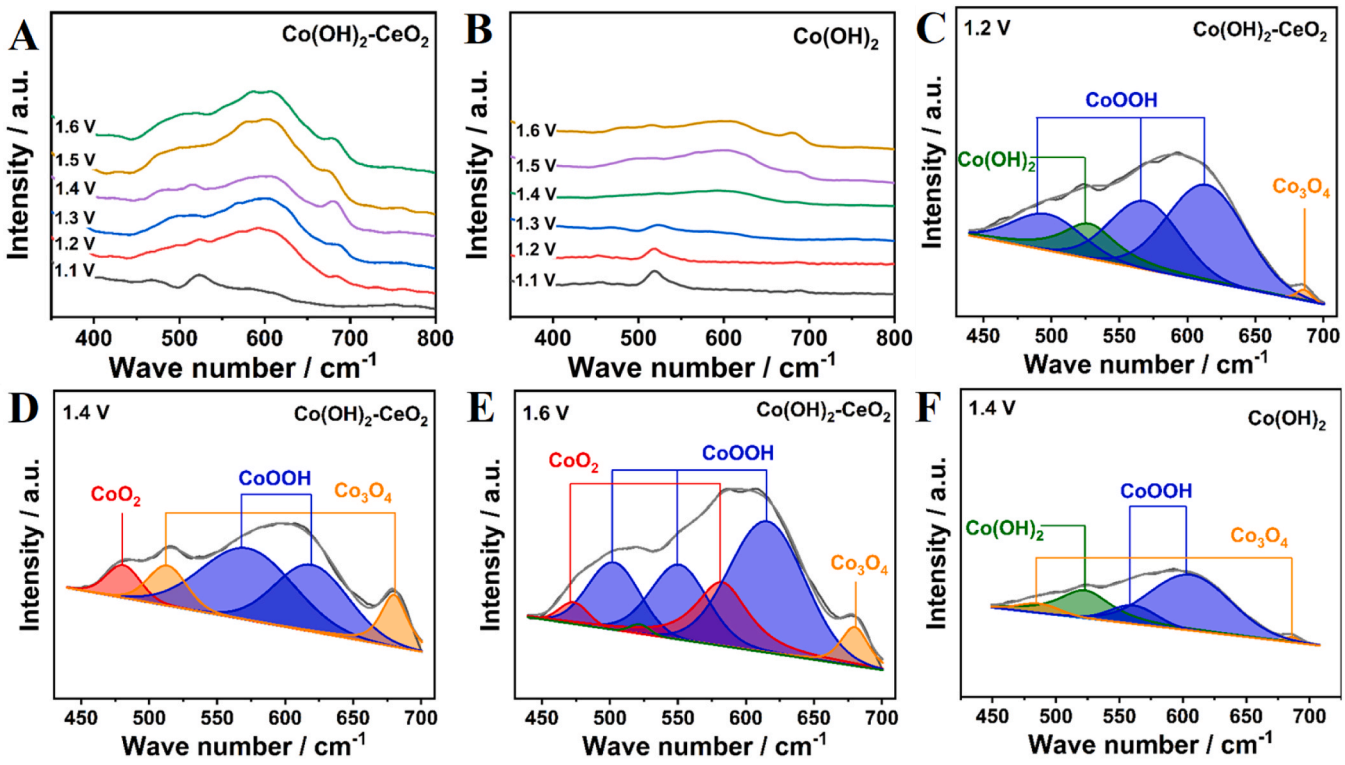

Fig. 6. In situ Raman spectra of $Co(OH)_2$-CeO_2 (A) and $Co(OH)_2$ (B) under different potential at pH 7, The Lorentz peak function fit of $Co(OH)_2$-CeO_2 at 1.2 V (C), 1.4 V (D) and 1.6 V (E), The Lorentz peak function fit of $Co(OH)_2$ at 1.4 V (F).

peaks have changed significantly. However, the Raman peaks do not change slightly until 1.3 V on $Co(OH)_2$ electrode (Fig. 6B). Therefore, we believe that the incorporation of CeO_2 has a strong impact on the evolution of the host active cobalt species. In order to analyze the changes of species more clearly, Lorentz fitting is performed on the Raman spectra at 1.2 V, 1.4 V and 1.6 V of $Co(OH)_2$-CeO_2, and the results are shown in Fig. 6C-E. At 1.2 V, the characteristic peaks corresponding to CoOOH appear at 489 cm^{-1}, 569 cm^{-1} and 612 cm^{-1}, and the characteristic peak of $Co(OH)_2$ still appears at 524 cm^{-1}, while the characteristic peak corresponding to Co_3O_4 appears at 686 cm^{-1}, indicating that the divalent Co species begin to transform to the higher valence Co species, mainly trivalent CoOOH. When the potential increases to 1.4 V, in addition to CoOOH at 569 cm^{-1} and 612 cm^{-1} and Co_3O_4 at 680 cm^{-1}, a characteristic peak corresponding to Co_3O_4 appears at 515 cm^{-1}, and a small amount of higher valence peak corresponding to CoO_2 appeared at 480 cm^{-1}, indicating that a certain amount of trivalent Co species was converted to tetravalent CoO_2 [48, 49]. With the further increase of the potential, the Raman spectrum at 1.6 V is shown in Fig. 6E, and the characteristic peaks of CoOOH are still retained at 501 cm^{-1} and 549 cm^{-1} and 614 cm^{-1}. There is also a certain amount of Co_3O_4 at 680 cm^{-1}, but it can be clearly seen that the characteristic peaks of CoO_2 appear at 476 cm^{-1} and 580 cm^{-1}. The results from electrochemical in situ Raman spectra show that the Co active species undergo the change of $Co(OH)_2$ → CoOOH → CoO_2 with the increase of potential, and CoOOH is the active species at low potential, while CoO_2 is the active species at high potential. Meanwhile, we perform Lorentz fitting on the Raman peak at 1.4 V of the $Co(OH)_2$ electrode to observe the active species. As shown in Fig. 6F, there is still a certain amount of $Co(OH)_2$ at 524 cm^{-1}. More importantly, the strength of CoOOH at 560 $cm^{-1}$and 608 cm^{-1} is far lower than that of $Co(OH)_2$ electrode at 1.4 V. Therefore, the induce of CeO_2 greatly promotes the conversion of main element Co to high-valent active species, which is responsible for the enhancement of HMFCA. In addition, we carried out the in situ electrochemical Raman test of $Co(OH)_2$-CeO_2 under the condition of pH = 10, and the results are shown in Fig. S7. It could be seen that when the potential is 1.2 V, the characteristic peaks corresponding to CoOOH and CoO_2 appear at 487 cm^{-1} and 589 cm^{-1}. With the increase of potential, the intensity of the characteristic peaks corresponding to CoO_2 between 467 and 480 cm^{-1} and 589 cm^{-1} increases. These results show that at high pH, Co^{3+} and Co^{4+} active cobalt species are generated at low potential, which makes both hydroxyl and aldehyde groups of HMF oxidized. That is the key difference from the

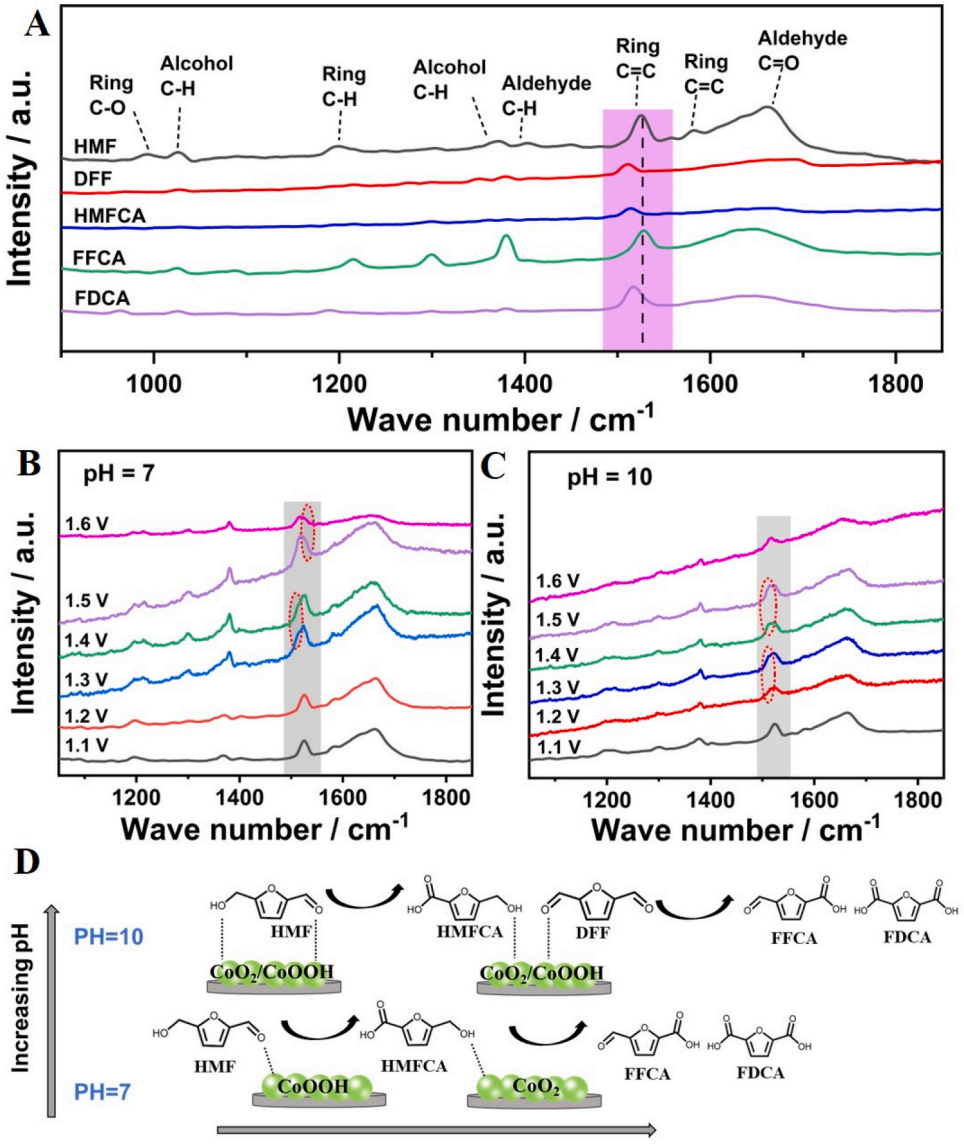

Fig. 7. Raman spectra of HMF and relevant intermediate (A). In situ Raman spectra of electrolyte change under different potential at pH 7 (B) and pH 10 (C). Schematic diagram of HMF conversion path on $Co(OH)_2$-CeO_2 catalyst at different pH and potentials (D).

selective oxidation of aldehyde groups to HMFCA by CoOOH at low pH value and low potential.

The evolution of reactants and products under different pH are also tracked to explore the selective conversion path of HMF on $Co(OH)_2$-CeO_2. Fig. 7A shows the in situ Raman spectra of five reactants and products of HMF, DFF, HMFCA, FFCA and FDCA. Since HMF is a structure with hydroxyl and aldehyde functional groups on a furan ring, it is difficult to distinguish the evolution of reactants and products by characteristic functional groups due to the overlap of functional groups with its electrocatalytic products. However, due to the electron-donating effect of the hydroxyl functional group and the electron-withdrawing effect of the aldehyde and carboxyl functional groups, the C = C vibration on the furan ring of the five substances will be slightly different. In HMF, the characteristic peak of C = C ring appears at 1523 cm^{-1}. In DFF, C = C ring appears at 1510 cm^{-1}. In HMFCA, C = C ring appears at 1515 cm^{-1}. In FFCA and FDCA, C = C ring appears at 1528 cm^{-1} and 1518 cm^{-1}, respectively [50,51]. Then we study the Raman changes of the solution at pH 7 and pH 10, and the results are shown in Figs. 7B and 7C. In the electrolysis system with pH of 7, there is no significant change in the reactants at 1.1 V and 1.2 V. When the potential increases to 1.3 V, a characteristic peak corresponding to HMFCA appears at 1515 cm^{-1}. When the potential further increases to 1.5 V, a characteristic peak corresponding to FFCA appears at 1528 cm^{-1}, indicating that HMF is electrocatalyzed to HMFCA through two-electron oxidation of aldehyde group under this solution condition, with the increase of potential, the hydroxyl group begin to be oxidized to FFCA and FDCA. In the electrolysis system of pH 10, a characteristic peak corresponding to HMFCA appears at 1515 cm^{-1} at 1.2 V, and a characteristic peak corresponding to DFF appears at 1510 cm^{-1} when the potential increases to 1.3 V. These indicate that hydroxyl oxidation can occur at low potential at high pH. HMF will be oxidized by hydroxyl and aldehyde to form DFF and HMFCA, FFCA and FDCA will be generated quickly with the increase of potential. According to the evolution process of active species and reactants obtained by electrochemical in situ Raman, we propose the transformation path of HMF with the change of potential and pH on $Co(OH)_2$-CeO_2 electrode, as shown in Fig. 7D. Under neutral conditions, the oxidation of hydroxyl groups (-COH) on HMF is inhibited and the large amount induced CoOOH reacts with aldehyde groups (-CHO) of HMF, realizing selective two-electron electrocatalytic conversion of HMF to HMFCA boosting hydrogen production. However, both hydroxyl and aldehyde groups are oxidized, resulting in the mixed formation of HMFCA and DFF at high pH. When further adjusting the applied potential, the evolution of CoOOH and CoO_2 active species can realize the selective electrooxidation of HMF with different degrees.

4. Conclusion

In summary, a $Co(OH)_2$-CeO_2 electrode is successfully prepared by a simple electrodeposition method and used as anode for the selective electrocatalytic conversion of HMF. The mild conversion of HMF to HMFCA through two-electron oxidation of aldehyde group is achieved at 1.4 V under neutral condition, with a selectivity of 89.4% and a yield of 85.8%. The coupled hydrogen production of the cathode at 1.4 V is 4.1 times that of pure water oxidation under neutral conditions, indicating that HMF oxidation could replace water oxidation to promote hydrogen production. At the same time, it is found that HMF mild oxidation could facilitate hydrogen production more than deep oxidation. Electrocatalytic measurements and in situ Raman spectroscopy show that the high and tunable electrocatalytic performance are attributed to the following features: i) Low pH and potential inhibit the oxidation of alcohol hydroxyl groups; ii) CeO_2 incorporation induced fast formation of Co^{3+} compounds are key active species to catalyze the selective electrocatalytic conversion of HMF to HMFCA through two-electron oxidation of aldehyde group; iii) Co^{4+} active species facilitate the oxidation of hydroxyl group to generate FFCA and FDCA. Our results provide feasible way in generating high-valued chemicals and hydrogen.

CRediT authorship contribution statement

Yanan Xie: Conceptualization, Formal analysis, Methodology, Investigation, Data curation, Writing-original draft, Writing-review & editing. **Lingzhi Sun:** Conceptualization, Validation, Formal analysis, Investigation. **Xun Pan:** Methodology, Investigation. **Zhaoyu Zhou:** Methodology, Investigation. **Guohua Zhao:** Supervision, Conceptualization, Funding acquisition.

Declaration of Competing Interest

The authors declare that they have no known competing financial interests or personal relationships that could have appeared to influence the work reported in this paper.

Data Availability

Data will be made available on request.

Acknowledgements

This work was financially supported by the National Natural Science Foundation of China (NSFC, No.22076140, 21876128, 21537003).

Appendix A. Supporting information

Supplementary data associated with this article can be found in the online version at doi:10.1016/j.apcatb.2023.123068.

References

[1] M.S. Dresselhaus, I.L. Thomas, Alternative energy technologies, Nature 414 (2001) 332, https://doi.org/10.1038/35104599.
[2] T.R. Cook, D.K. Dogutan, S.Y. Reece, S. Yogesh, S.T. Thomas, D.G. Nocera, Solar energy supply and storage for the legacy and nonlegacy worlds, Chem. Rev. 110 (2010) 6474–6502, https://doi.org/10.1021/cr100246c.
[3] J. Zhang, T. Wang, P. Liu, Z. Liao, S. Liu, X. Zhuang, M. Chen, E. Zschech, X. Feng, Efficient hydrogen production on MoNi4 electrocatalysts with fast water dissociation kinetics, Nat. Commun. 8 (2017) 15437, https://doi.org/10.1038/ncomms15437.
[4] X. Wei, S. Wang, Z. Hua, L. Chen, J. Shi, Metal-organic framework nanosheet electrocatalysts for efficient H2 production from methanol solution: methanol-assisted water splitting or methanol reforming? ACS Appl. Mater. Interfaces 10 (2018) 25422–25428, https://doi.org/10.1021/acsami.8b06948.
[5] W. Zhu, M. Ren, N. Hu, W. Zhang, Z. Luo, R. Wang, J. Wang, L. Huang, Y. Suo, J. Wang, Traditional NiCo2S4 phase with porous nanosheets array topology on carbon cloth: a flexible, versatile and fabulous electrocatalyst for overall water and urea electrolysis, ACS Sustain. Chem. Eng. 6 (2018) 5011–5020, https://doi.org/10.1021/acssuschemeng.7b04663.
[6] Y. Li, X. Wei, L. Chen, J. Shi, M. He, Nickel-molybdenum nitride nanoplate electrocatalysts for concurrent electrolytic hydrogen and formate productions, Nat. Commun. 10 (2019) 5335, https://doi.org/10.1038/s41467-019-13375-z.
[7] A.A. Rosatella, S.P. Simeonov, R.F.M. Frade, C.A.M. Afonso, 5-Hydroxymethylfurfural (HMF) as a building block platform: Biological properties, synthesis and synthetic applications, Green. Chem. 13 (2011) 754–793, https://doi.org/10.1039/c0gc00401d.
[8] B.M. Matsagar, M.K. Munshi, A.A. Kelkar, P.L. Dhepe, Conversion of concentrated sugar solutions into 5-hydroxymethyl furfural and furfural using Brönsted acidic ionic liquids, Catal. Sci. Technol. 5 (2015) 5086–5090, https://doi.org/10.1039/c5cy00858a.
[9] L. Hu, G. Zhao, W. Hao, X. Tang, Y. Sun, L. Lin, S. Liu, Catalytic conversion of biomass-derived carbohydrates into fuels and chemicals via furanic aldehydes, RSC Adv. 2 (2012) 11184–11206, https://doi.org/10.1039/c2ra21811a.
[10] J.J. Bozell, G.R. Petersen, Technology development for the production of biobased products from biorefinery carbohydrates—the US Department of Energy's "Top 10" revisited, Green. Chem. 12 (2010) 539, https://doi.org/10.1039/b922014c.
[11] X. Tong, Y. Ma, Y. Li, Biomass into chemicals: conversion of sugars to furan derivatives by catalytic processes, Appl. Catal. A: Gen. 385 (2010) 1–13, https://doi.org/10.1016/j.apcata.2010.06.049.
[12] B. You, N. Jiang, X. Liu, Y. Sun, Simultaneous H2 generation and biomass upgrading in water by an efficient noble-metal-free bifunctional electrocatalyst, Angew. Chem. Int. Ed. Engl. 55 (2016) 9913–9917, https://doi.org/10.1002/anie.201603798.

[13] B. You, X. Liu, N. Jiang, Y. Sun, A general strategy for decoupled hydrogen production from water splitting by integrating oxidative biomass valorization, J. Am. Chem. Soc. 138 (2016) 13639–13646, https://doi.org/10.1021/jacs.6b07127.
[14] B. You, X. Liu, X. Liu, Y. Sun, Efficient H2 evolution coupled with oxidative refining of alcohols via a hierarchically porous nickel bifunctional electrocatalyst, ACS Catal. 7 (2017) 4564–4570, https://doi.org/10.1021/acscatal.7b00876.
[15] Y. Xie, Z. Zhou, N. Yang, G. Zhao, An overall reaction integrated with highly selective oxidation of 5–hydroxymethylfurfural and efficient hydrogen evolution, Adv. Funct. Mater. 31 (2021) 2102886, https://doi.org/10.1002/adfm.202102886.
[16] C. Liu, M. Hirohara, T. Maekawa, R. Chang, T. Hayashi, C.-Y. Chiang, Selective electro-oxidation of glycerol to dihydroxyacetone by a non-precious electrocatalyst – CuO, Appl. Catal. B: Environ. 265 (2020), 118543, https://doi.org/10.1016/j.apcatb.2019.118543.
[17] Y. Lu, T. Liu, C.L. Dong, C. Yang, L. Zhou, Y.C. Huang, Y. Li, B. Zhou, Y. Zou, S. Wang, Tailoring competitive adsorption sites by oxygen-vacancy on cobalt oxides to enhance the electrooxidation of biomass, Adv. Mater. 34 (2022), e2107185, https://doi.org/10.1002/adma.202107185.
[18] X. Han, H. Sheng, C. Yu, T.W. Walker, G.W. Huber, J. Qiu, S. Jin, Electrocatalytic oxidation of glycerol to formic acid by CuCo2O4 spinel oxide nanostructure catalysts, ACS Catal. 10 (2020) 6741–6752, https://doi.org/10.1021/acscatal.0c01498.
[19] A.V. Munde, B.B. Mulik, P.P. Chavan, V.S. Sapner, S.S. Narwade, S.M. Mali, B. R. Sathe, Electrocatalytic ethanol oxidation on cobalt-bismuth nanoparticle-decorated reduced graphene oxide (Co-Bi@rGO): reaction pathway investigation toward direct ethanol fuel cells, J. Phys. Chem. C. 125 (2021) 2345–2356, https://doi.org/10.1021/acs.jpcc.0c10668.
[20] J. Xu, X. Liu, Y. Chen, Y. Zhou, T. Lu, Y. Tang, Platinum-Cobalt alloy networks for methanol oxidation electrocatalysis, J. Mater. Chem. 22 (2012) 23659, https://doi.org/10.1039/c2jm35649j.
[21] A. Ashok, A. Kumar, Ag/Co3O4 as an effective catalyst for glycerol electro-oxidation in alkaline medium, Int. J. Hydrog. Energy 46 (2021) 4788–4797, https://doi.org/10.1016/j.ijhydene.2020.04.118.
[22] X. Deng, G.Y. Xu, Y.J. Zhang, L. Wang, J. Zhang, J.F. Li, X.Z. Fu, J.L. Luo, Understanding the roles of electrogenerated Co3+ and Co4+ in Selectivity-Tuned 5-Hydroxymethylfurfural oxidation, Angew. Chem. Int. Ed. Engl. 60 (2021) 20535–20542, https://doi.org/10.1002/anie.202108955.
[23] W. Wu, Z.-H. Huang, T.-T. Lim, Recent development of mixed metal oxide anodes for electrochemical oxidation of organic pollutants in water, Appl. Catal. A: Gen. 480 (2014) 58–78, https://doi.org/10.1016/j.apcata.2014.04.035.
[24] H.S. Jadhav, A. Roy, W.-J. Chung, J.G. Seo, Free standing growth of MnCo2O4 nanoflakes as an electrocatalyst for methanol electro-oxidation, N. J. Chem. 41 (2017) 15058–15063, https://doi.org/10.1039/c7nj03180g.
[25] A. Ashok, A. Kumar, J. Ponraj, S.A. Mansour, F. Tarlochan, Single step synthesis of porous NiCoO2 for effective electrooxidation of glycerol in alkaline medium, J. Electrochem. Soc. 165 (2018) J3301–J3309, https://doi.org/10.1149/2.0401815jes.
[26] L. Pan, Q. Wang, Y. Li, C. Zhang, Amorphous cobalt-cerium binary metal oxides as high performance electrocatalyst for oxygen evolution reaction, J. Catal. 384 (2020) 14–21, https://doi.org/10.1016/j.jcat.2020.02.005.
[27] Y. Liu, C. Ma, Q. Zhang, W. Wang, P. Pan, L. Gu, D. Xu, J. Bao, Z. Dai, 2D electron gas and oxygen vacancy induced high oxygen evolution performances for advanced Co3O4/CeO2 nanohybrids, Adv. Mater. 31 (2019), e1900062, https://doi.org/10.1002/adma.201900062.
[28] S.K. Godlaveeti, H. Maseed, S.A. Reddy, R.R. Nagireddy, Electrochemical performance of ternary RGO/β-Ni(OH)2/CeO2 composite in addition with different metal oxides for supercapacitor application, Adv. Nat. Sci.: Nanosci. Nanotechnol. 11 (2020), 025021, https://doi.org/10.1088/2043-6254/ab8bde.
[29] N. Yao, R. Meng, F. Wu, Z. Fan, G. Cheng, W. Luo, Oxygen-vacancy-Induced CeO2/Co4N heterostructures toward enhanced pH-universal hydrogen evolution reactions, Appl. Catal. B: Environ. 277 (2020), 119282, https://doi.org/10.1016/j.apcatb.2020.119282.
[30] Q. Gao, Y. Cui, S. Wang, B. Liu, C. Liu, Efficient activation of peroxymonosulfate by Co-doped mesoporous CeO2 nanorods as a heterogeneous catalyst for phenol oxidation, Environ. Sci. Pollut. Res Int 28 (2021) 27852–27863, https://doi.org/10.1007/s11356-021-12605-6.
[31] Y. Zhang, R. Xiao, S. Wang, H. Zhu, H. Song, G. Chen, H. Lin, J. Zhang, J. Xiong, Oxygen vacancy enhancing Fenton-like catalytic oxidation of norfloxacin over prussian blue modified CeO2: performance and mechanism, J. Hazard. Mater. 398 (2020), 122863, https://doi.org/10.1016/j.jhazmat.2020.122863.
[32] M.-C. Sung, G.-H. Lee, D.-W. Kim, CeO2/Co(OH)2 hybrid electrocatalysts for efficient hydrogen and oxygen evolution reaction, J. Alloy. Compd. 800 (2019) 450–455, https://doi.org/10.1016/j.jallcom.2019.06.047.
[33] Z. Liu, N. Li, H. Zhao, Y. Zhang, Y. Huang, Z. Yin, Y. Du, Regulating the active species of Ni(OH)2 using CeO2:3DCeO2/Ni(OH)2/carbon foam as an efficient electrode for the oxygen evolution reaction, Chem. Sci. 8 (2017) 3211–3217, https://doi.org/10.1039/c6sc05408k.
[34] H. Zhang, Y. Chen, L. Bao, J.Y. Ge, CeO2-CDs clusters decorated Co(OH)2 nanosheets for improved photocatalytic ammonia synthesis, J. Colloid Interface Sci. 634 (2023) 642–650, https://doi.org/10.1016/j.jcis.2022.12.065.
[35] S. Tiwari, N. Balasubramanian, S. Biring, S. Sen, Effect of Co doping on structural and mechanical properties of CeO2, AIP Conf. Proc. 1966 (2018), 020037, https://doi.org/10.1063/1.5038716.
[36] W. Li, D. Liu, X. Feng, Z. Zhang, X. Jin, Y. Zhang, High-Performance Ultrathin Co3O4 nanosheet supported PdO/CeO2 catalysts for methane combustion, Adv. Energy Mater. 9 (2019) 1803583, https://doi.org/10.1002/aenm.201803583.
[37] H. Palneedi, V. Mangam, S. Das, K. Das, Effect of fuel-to-nitrate ratio on the powder characteristics of nanosized CeO2 synthesized by mixed fuel combustion method, J. Alloy. Compd. 509 (2011) 9912–9918, https://doi.org/10.1016/j.jallcom.2011.07.087.
[38] B. Zhu, C. Chen, L. Huai, Z. Zhou, L. Wang, J. Zhang, 2,5-Bis(hydroxymethyl)furan: A new alternative to HMF for simultaneously electrocatalytic production of FDCA and H2 over CoOOH/Ni electrodes, Appl. Catal. B: Environ. 297 (2021), 120396, https://doi.org/10.1016/j.apcatb.2021.120396.
[39] J. Woo, B.C. Moon, U. Lee, H.-S. Oh, K.H. Chae, Y. Jun, B.K. Min, D.K. Lee, Collaborative electrochemical oxidation of the alcohol and aldehyde groups of 5-hydroxymethylfurfural by NiOOH and Cu(OH)2 for superior 2,5-furandicarboxylic acid production, ACS Catal. 12 (2022) 4078–4091, https://doi.org/10.1021/acscatal.1c05341.
[40] Y. Song, S. Jiang, Y. He, Y. Wu, X. Wan, W. Xie, J. Wang, Z. Li, H. Duan, M. Shao, Metal vacancy-enriched layered double hydroxide for biomass molecule electrooxidation coupled with hydrogen production, Fundam. Res. 14 (2022) 19, https://doi.org/10.1016/j.fmre.2022.05.023.
[41] H. Liu, T.-H. Lee, Y. Chen, E.W. Cochran, W. Li, Paired electrolysis of 5-(hydroxymethyl)furfural in flow cells with a high-performance oxide-derived silver cathode, Green. Chem. 23 (2021) 5056–5063, https://doi.org/10.1039/d1gc00988e.
[42] W.J. Liu, Z. Xu, D. Zhao, X.Q. Pan, H.C. Li, X. Hu, Z.Y. Fan, W.K. Wang, G.H. Zhao, S. Jin, G.W. Huber, H.Q. Yu, Efficient electrochemical production of glucaric acid and H2 via glucose electrolysis, Nat. Commun. 11 (2020) 265, https://doi.org/10.1038/s41467-019-14157-3.
[43] J. Na, B. Seo, J. Kim, C.W. Lee, H. Lee, Y.J. Hwang, B.K. Min, D.K. Lee, H.S. Oh, U. Lee, General technoeconomic analysis for electrochemical coproduction coupling carbon dioxide reduction with organic oxidation, Nat. Commun. 10 (2019) 5193, https://doi.org/10.1038/s41467-019-12744-y.
[44] Y. Wu, J. Zhao, C. Wang, T. Li, B.H. Zhao, Z. Song, C. Liu, B. Zhang, Electrosynthesis of a nylon-6 precursor from cyclohexanone and nitrite under ambient conditions, Nat. Commun. 14 (2023) 3057, https://doi.org/10.1038/s41467-023-38888-6.
[45] K.T.V. Rao, J.L. Rogers, S. Souzanchi, L. Dessbesell, M.B. Ray, C.C. Xu, Inexpensive but highly efficient Co-Mn mixed-oxide catalysts for selective oxidation of 5-Hydroxymethylfurfural to 2,5-Furandicarboxylic Acid, ChemSusChem 11 (2018) 3323–3334, https://doi.org/10.1002/cssc.201800989.
[46] T. Wang, Z. Huang, T. Liu, L. Tao, J. Tian, K. Gu, X. Wei, P. Zhou, L. Gan, S. Du, Y. Zou, R. Chen, Y. Li, X.Z. Fu, S. Wang, Transforming electrocatalytic biomass upgrading and hydrogen production from electricity input to electricity output, e202115636, Angew. Chem. Int. Ed. Engl. 61 (2022), https://doi.org/10.1002/anie.202115636.
[47] T. Wang, L. Tao, X. Zhu, C. Chen, W. Chen, S. Du, Y. Zhou, B. Zhou, D. Wang, C. Xie, P. Long, W. Li, Y. Wang, R. Chen, Y. Zou, X.-Z. Fu, Y. Li, X. Duan, S. Wang, Combined anodic and cathodic hydrogen production from aldehyde oxidation and hydrogen evolution reaction, Nat. Catal. 5 (2022) 66–73, https://doi.org/10.1038/s41929-021-00721-y.
[48] W. Li, L. Zhao, C. Wang, X. Lu, W. Chen, Interface engineering of heterogeneous CeO2-CoO nanofibers with rich oxygen vacancies for enhanced electrocatalytic oxygen evolution performance, ACS Appl. Mater. Interfaces 13 (2021) 46998–47009, https://doi.org/10.1021/acsami.1c11101.
[49] H. Sun, C. Tian, G. Fan, J. Qi, Z. Liu, Z. Yan, F. Cheng, J. Chen, C.P. Li, M. Du, Boosting activity on Co4N porous nanosheet by coupling CeO2 for efficient electrochemical overall water splitting at high current densities, Adv. Funct. Mater. 30 (2020) 1910596, https://doi.org/10.1002/adfm.201910596.
[50] T.-G. Vo, P.-Y. Ho, C.-Y. Chiang, Operando mechanistic studies of selective oxidation of glycerol to dihydroxyacetone over amorphous cobalt oxide, Appl. Catal. B: Environ. 300 (2022), 120723, https://doi.org/10.1016/j.apcatb.2021.120723.
[51] Y. Hu, C. Hu, A. Du, T. Xiao, L. Yu, C. Yang, W. Xie, Interfacial evolution on Co-based oxygen evolution reaction electrocatalysts probed by using in situ surface-enhanced raman spectroscopy, Anal. Chem. 95 (2023) 1703–1709, https://doi.org/10.1021/acs.analchem.2c04931.
[52] N. Yao, G. Wang, H. Jia, J. Yin, H. Cong, S. Chen, W. Luo, Intermolecular energy gap-induced formation of high-valent cobalt species in CoOOH surface layer on cobalt sulfides for efficient water oxidation, Angew. Chem. Int. Ed. Engl. 61 (2022), e202117178, https://doi.org/10.1002/anie.202117178.
[53] H. Wang, Y. Zhou, S. Tao, CoP-CoOOH heterojunction with modulating interfacial electronic structure: a robust biomass-upgrading electrocatalyst, Appl. Catal. B: Environ. 315 (2022), 121588, https://doi.org/10.1016/j.apcatb.2022.121588.
[54] H. Wang, C. Li, J. An, Y. Zhuang, S. Tao, Surface reconstruction of NiCoP for enhanced biomass upgrading, J. Mater. Chem. A 9 (2021) 18421–18430, https://doi.org/10.1039/d1ta05425b.